

## Development of pH/Glutathione Responsive Theranostic Agents Activated by Glutathione S-transferase # for Human Colon Cancer

Ji Liu, Xin Liu, Jianqiang Qian, Chi Meng, Peng Zhu, Jiaying Hang, Yaling Wang, biao xiong, Xiaodong Qiu, Weizhong Zhu, Yumin Yang, Yanan Zhang, and Yong Ling

*J. Med. Chem.*, **Just Accepted Manuscript** • DOI: 10.1021/acs.jmedchem.0c00354 • Publication Date (Web): 05 Aug 2020

Downloaded from [pubs.acs.org](https://pubs.acs.org) on August 6, 2020

### Just Accepted

“Just Accepted” manuscripts have been peer-reviewed and accepted for publication. They are posted online prior to technical editing, formatting for publication and author proofing. The American Chemical Society provides “Just Accepted” as a service to the research community to expedite the dissemination of scientific material as soon as possible after acceptance. “Just Accepted” manuscripts appear in full in PDF format accompanied by an HTML abstract. “Just Accepted” manuscripts have been fully peer reviewed, but should not be considered the official version of record. They are citable by the Digital Object Identifier (DOI®). “Just Accepted” is an optional service offered to authors. Therefore, the “Just Accepted” Web site may not include all articles that will be published in the journal. After a manuscript is technically edited and formatted, it will be removed from the “Just Accepted” Web site and published as an ASAP article. Note that technical editing may introduce minor changes to the manuscript text and/or graphics which could affect content, and all legal disclaimers and ethical guidelines that apply to the journal pertain. ACS cannot be held responsible for errors or consequences arising from the use of information contained in these “Just Accepted” manuscripts.

# Development of pH/Glutathione Responsive Theranostic Agents Activated by Glutathione S-transferase $\pi$ for Human Colon Cancer

Ji Liu<sup>a,#</sup>, Xin Liu<sup>a,#</sup>, Jianqiang Qian<sup>a</sup>, Chi Meng<sup>a</sup>, Peng Zhu<sup>a,b</sup>, Jiaying Hang<sup>a</sup>, Yaling Wang<sup>a,b</sup>,  
Biao Xiong<sup>a</sup>, Xiaodong Qiu<sup>a</sup>, Weizhong Zhu<sup>a</sup>, Yumin Yang<sup>b</sup>, Yanan Zhang<sup>a,\*</sup>, Yong Ling<sup>a,b,\*</sup>

<sup>a</sup>School of Pharmacy and Jiangsu Province Key Laboratory for Inflammation and Molecular Drug Target, Nantong University, Nantong 226001, PR China.

<sup>b</sup>Key Laboratory of Neuroregeneration, Ministry of Education and Jiangsu Province, Co-innovation Center of Neuroregeneration, Nantong University, Nantong 226001, PR China

**Abstract:** Two novel theranostic agents **HJTA** and **HJTB** have been designed and synthesized by covalently linking a  $\beta$ -carboline derivative, with anti-tumor activities and pH responsive fluorescence, with a 2-exomethylenecyclohexanone moiety which can be activated by the tumor-targeting glutathione (GSH)/glutathione S-transferase  $\pi$  (GST $\pi$ ). These agents displayed pH- and GSH- dual responsive fluorescence in tumor cells but not in normal cells. Importantly, **HJTA** selectively illuminated tumor tissue for up to 7h, and generated precise visualization of orthotopic colonic tumors through the blood circulation system in intraoperative mice. Further, **HJTA** exhibited potent and selective antiproliferative activities and colonic tumor inhibition in mice. Finally, **HJTA** induced great cancer cell apoptosis and autophagy by regulating expression of apoptotic and autophagic proteins. Therefore, this pH/GSH dual responsive fluorescent probe with cancer-targeting therapeutic activity provides a novel tool for precise diagnosis and tumor treatment, therefore broadening the impact of multifunctional agents as theranostic precision medicines.

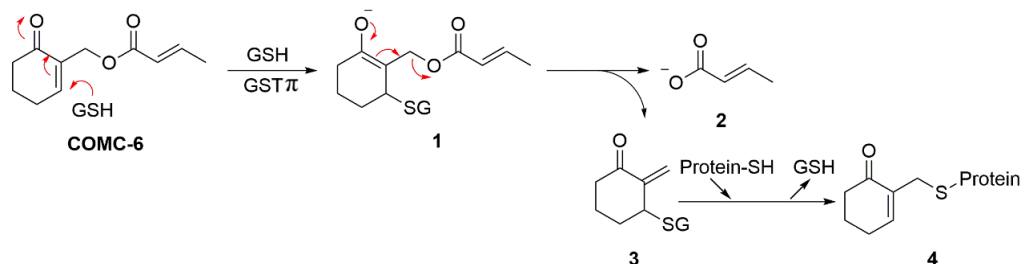
**Keywords:**  $\beta$ -Carbolines, Glutathione transferase  $\pi$ , pH/GSH dual responsive fluorescence, Selective tumor suppression, Tumor microenvironment

## 1. Introduction

Tumor microenvironment (TME), the special environment formed by the interactions between tumor cells and cell surroundings during the tumor cells growth process,<sup>1,2</sup> plays a pivotal role during tumor initiation, progression, and metastasis, and significantly influences therapeutic response and clinical outcome.<sup>3</sup> The differences on the physical and chemical properties of tumor microenvironment from normal tissue,<sup>4,6</sup> have been widely targeted for the development of targeted therapy in order to improve efficacy and reduce side effects. One of the main differences is the up-regulated oxidative stress in TME, resulting from the over-activation of reactive oxygen species (ROS) under anoxic conditions in different TME associated cells.<sup>7,8</sup> The excessive ROS formation in TME can cause cell damage and even death,<sup>9</sup> and therefore, antioxidant systems are concomitantly upregulated in order to maintain redox homeostasis.<sup>10</sup> Glutathione (GSH) is the main antioxidant involved in maintaining this redox balance through direct scavenging of peroxides and free radicals,<sup>11,12</sup> and elevated concentrations of intracellular GSH have been found in many types of human tumor tissues.<sup>13</sup> The human glutathione transferase  $\pi$  isozyme (GST $\pi$ ) is a key member of the family of glutathione transferase (GST) proteins that catalyze the nucleophilic attack and conjugation of GSH with reactive electrophiles. GST $\pi$  is overexpressed in many cancer cells,<sup>14</sup> such as breast and colon cancer,<sup>15,16</sup> and in drug-resistant tumors,<sup>17</sup> and is associated with cell carcinogenesis, tumor formation and drug resistance of human tissues.

The GSH-rich TME has been a target for anti-tumor medications development. Studies have shown that (6-oxocyclohex-1-en-1-yl)methyl (E)-but-2-enoate (COMC-6) and its analogues, all promising anticancer agents against human tumors,<sup>18</sup> interact with the over-expressed GST $\pi$  in various tumor cells. When catalyzed by GST $\pi$ , GSH conjugates with COMC-6 leading to a GSH

addition product **1**, which subsequently fragments to 2-exomethylene-3-glutathionyl-cyclohexanone **3** and crotonic acid.<sup>19</sup> The active intermediate **3** can combine with thiols on DNA or proteins via covalent bonds in many tumor cells, therefore generating marked anticancer effect (Scheme 1).<sup>20</sup>



**Scheme 1.** Reaction Mechanism of COMC-6 with GSH/GST $\pi$ .

In addition, TME is also associated with lower extracellular pH than normal tissue environment as well as lower intracellular lysosomal pH.<sup>21-24</sup> This weak acidic extracellular environment around tumor tissues results from the Warburg Effect, where the metabolism is altered with the rate of glucose uptake increasing and lactate being produced, and could facilitate the invasion, mutation, metastasis, and multi-drug resistance of the tumor.<sup>25-27</sup> This characteristic of TME has also been specifically targeted by many research teams. As a result, a variety of pH responsive probes have been developed to study various tumor processes in cells and in animals,<sup>28</sup> although they are mainly based on nanoparticles thus far.<sup>29</sup>

Here we describe our efforts in the development of theranostics, agents that combine therapy with diagnostics, that simultaneously target the over-expressed GST $\pi$  and the acidic TME of the tumors. Such rationally designed theranostic agents, in addition to providing targeted treatment, would also allow imaging of the cancer site and determining biodistribution of the drug. Our group has recently developed several series of promising antitumor agents based on the naturally occurring  $\beta$ -carboline,<sup>30-32</sup> a class of compounds that possess anticancer activities and also have fluorescence because of the highly conjugated planar polyaromatic structure. Interestingly, we found for the first time that the fluorescence of these substituted  $\beta$ -carboline derivatives was highly pH-dependent, only present at acidic pH. Therefore, we examined the possibility of

generating novel theranostic agents by replacing the crotonic acid by a  $\beta$ -carboline moiety with pH-responsive fluorescence properties to provide a novel class of 2-exomethylenecyclohexanones (**HJTA** and **HJTB**, Figure 1). Upon reaction with GSH and GST $\pi$ , the active molecules **3** and  $\beta$ -carbolines will be liberated (Figure 1). Given the antiproliferative properties of both COMC-6 and  $\beta$ -carbolines and their ability to detect and illuminate tissues with special pH's as in the TME, these novel agents may serve as excellent theranostic agents to provide *in-vivo* and real-time diagnosis of tumor tissue and TME intraoperatively, as well as possessing chemotherapeutic capability to prevent recurrence of residual tumor and improve patient outcome.

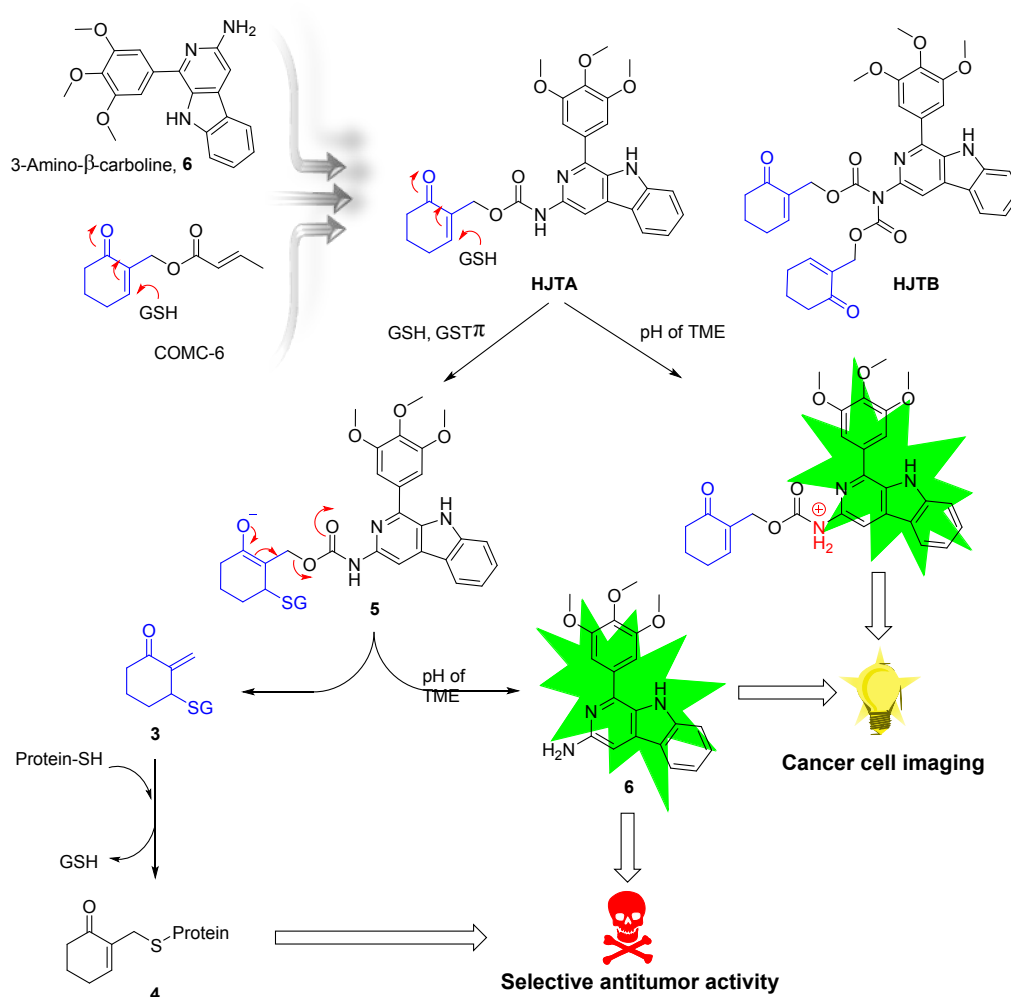
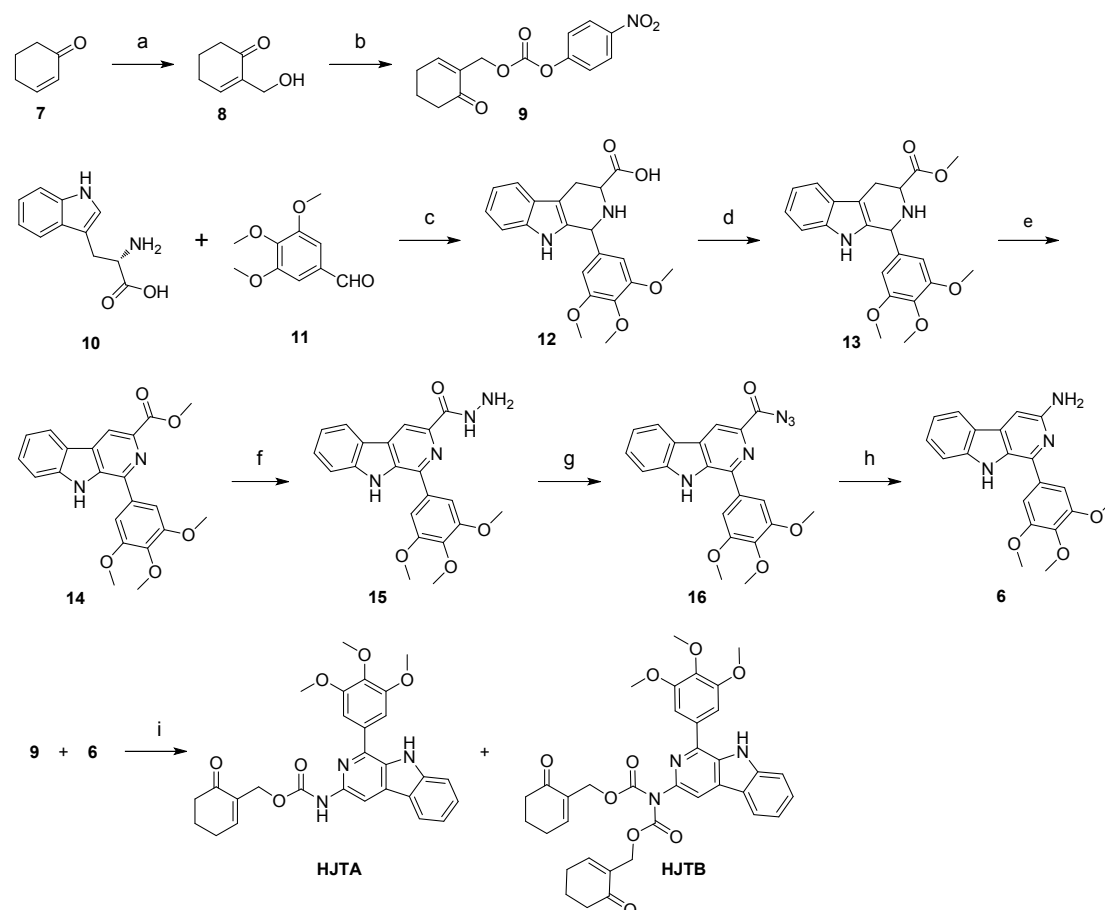


**Figure 1.** Schematic illustration of constructing and activation the tumor-targeting and pH and GSH/GST $\pi$  dependent probes **HJTA** and **HJTB**.

## 2. Results and Discussion

### 2.1 Synthesis of **HJTA** and **HJTB**

1  
2  
3 The synthetic scheme of **HJTA** and **HJTB** is presented in Scheme 2. The starting  
4 cyclohex-2-en-1-one **7** and formaldehyde were reacted to provide  
5 2-(hydroxymethyl)cyclohex-2-en-1-one **8** by a Baylis–Hillman reaction. Intermediate **8** then  
6  
7 reacted with 4-nitrophenyl chloroformate to provide compound **9**. Separately, the tricyclic system  
8  
9 of tetrahydron- $\beta$ -carboline parent ring **12** was constructed via a Pictet–Spengler reaction between  
10  
11 L-tryptophane **10** and 3,4,5-trimethoxybenzaldehyde **11**. Compound **12** was transformed to the ester  
12  
13 **13** under classical esterification conditions using  $\text{SOCl}_2$  and  $\text{CH}_3\text{OH}$ . The oxidization of ester **13**  
14  
15 with  $\text{KMnO}_4$  in a DMF solution afforded compound **14**, which was further treated with hydrazine  
16  
17 monohydrate to provide **15**. Hydrazide compound **15** was then converted to acyl azide **16** using  
18  
19 sodium nitrite. Then the acyl azide group of **16** was transformed to an amino group in an aqueous  
20  
21 acetic acid solution by the Curtis rearrangement reaction to afford 3-amino- $\beta$ -carboline **6**. Finally,  
22  
23 **HJTA** and **HJTB** were constructed via an amidation reaction between 3-amino- $\beta$ -carboline **6** and  
24  
25 intermediate **9** in the presence of DIPEA. The final compounds **HJTA** and **HJTB** were  
26  
27 characterized by  $^1\text{H}$  NMR,  $^{13}\text{C}$  NMR, and ESI mass spectrometry (Figure S7–S13, Supporting  
28  
29 Information).  
30  
31  
32  
33  
34  
35  
36  
37  
38  
39  
40  
41  
42  
43  
44  
45  
46  
47  
48  
49  
50  
51  
52  
53  
54  
55  
56  
57  
58  
59  
60



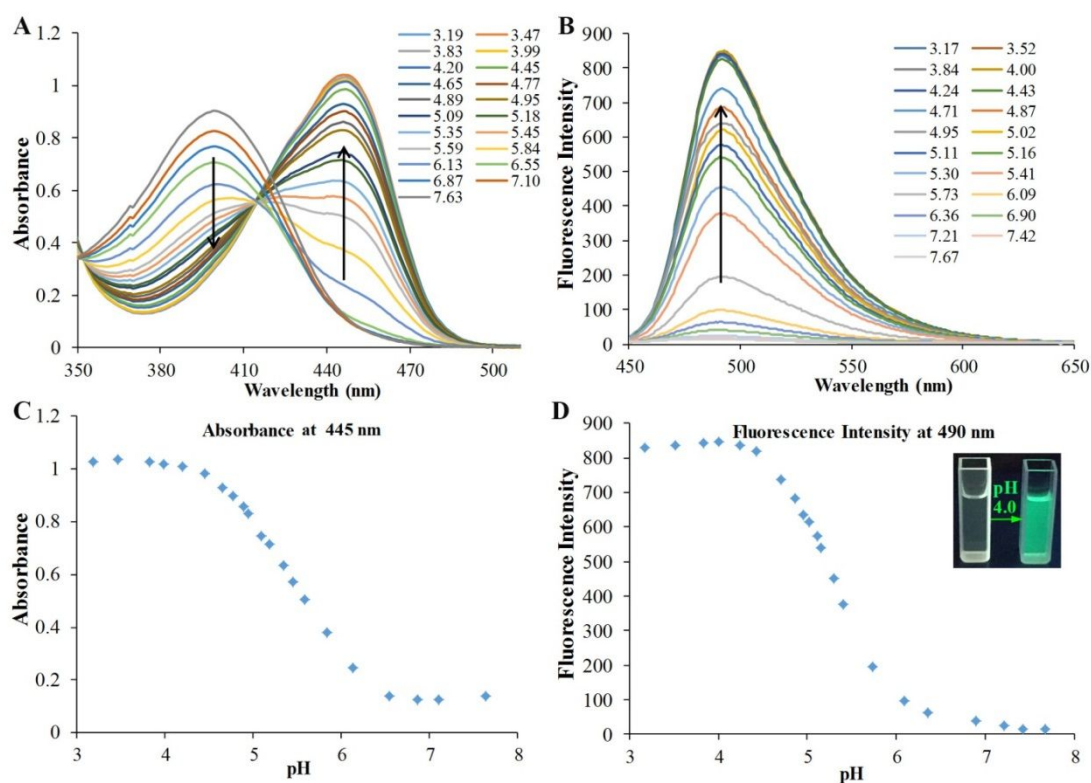
**Scheme 2.** Synthetic scheme for **HJTA** and **HJTB**. (a) HCHO, DMAP, 18 h, 86%; (b) 4-nitrophenyl carbonochloridate, DIPEA, CH<sub>2</sub>Cl<sub>2</sub>, 0 °C, 2 h, 70%; (c) HAc, 100 °C, 4 h, 84%; (d) SOCl<sub>2</sub>, Methanol, -5 °C, 1 h, and then reflux 5 h, 89%; (e) KMnO<sub>4</sub>, DMF, reflux, 4 h, 69%; (f) NH<sub>2</sub>-NH<sub>2</sub>·H<sub>2</sub>O, Methanol, 0 °C, 1 h, 95%; (g) NaNO<sub>2</sub>, HCl aqueous solution, 0 °C, 6 h; (h) HAc aqueous solution, reflux, 6h, 71%; (i) DIPEA, CH<sub>2</sub>Cl<sub>2</sub>, 0 °C, 4 h, 40% and 28%.

## 2.2 pH response of 6, HJTA, and HJTB

In order to confirm that the newly synthesized agents **HJTA** and **HJTB** have the same pH-responsiveness that was observed with the 3-amino-β-carboline subunit **6**, these compounds were first evaluated using both UV-vis absorption and fluorescence emission spectroscopy. To our delight, 3-amino-β-carboline **6** exhibited remarkable pH-responsiveness from pH 3 to 7 through an internal charge transfer (ICT) process (Figure S1). We then probed the pH-responsive properties of **HJTA** and **HJTB**. As shown in Figure 2A, as the pH decreased from 7.63 to 3.19, the absorption band of **HJTA** gradually shifted from 398 to 445 nm, with a distinct isosbestic point observed at 416 nm. The fluorescence intensity at 490 nm underwent a concomitant monotonic

1  
2  
3 increase (Figure 2B). However, the fluorescence was fully quenched in an aqueous solution with  
4 neutral pH. A quantitative analysis of the fluorescence intensity at 490 nm vs. pH (Figure 2D)  
5 revealed a 65-fold (from  $845.348 \pm 12.47$  to  $13.035 \pm 1.26$ ) increase as the pH was lowered from  
6 7.67 to 3.17. The pKa of **HJTA** was calculated to be 5.2 (Figure S2) and the relative  
7 fluorescence-quantum yield is 0.63 at pH 4.0, compared with Quinine sulfate (Table S1).<sup>33</sup>  
8  
9  
10  
11  
12

13 Similarly, the photophysical characteristics of **HJTB** were also measured under different pH's.  
14 A 50 nm red-shift with a distinct isosbestic point was observed at 418 nm and enhancement of  
15 absorption at 447 nm occurred with the decrease of pH from 7.62 to 3.21. Similar to **HJTA**, a  
16 60-fold enhancement of fluorescent intensity at 490 nm was also obtained with the decrease of pH  
17 when excited at 447 nm. The pKa value of **HJTB** was 5.3 (Figure S3), which falls in the pH range  
18 of TME over normal tissue. The relative fluorescence-quantum yield is 0.67 at pH 4.0, compared  
19 with Quinine sulfate (Table S1).<sup>33</sup> These results support that the pH-dependent fluorescent  
20 properties are retained in these  $\beta$ -carboline based designed probes which are suitable for  
21 visualizing TME. The relative fluorescence-quantum yield is 0.67 at pH 4.0, compared  
22 with Quinine sulfate (Table S1).<sup>33</sup> These results support that the pH-dependent fluorescent  
23 properties are retained in these  $\beta$ -carboline based designed probes which are suitable for  
24 visualizing TME.  
25  
26  
27  
28  
29  
30  
31



57 **Figure 2.** (A) Absorption spectra of **HJTA** (100  $\mu$ M) at different pH (7.63 - 3.19) in an aqueous  
58 solution containing 1% (v/v) DMSO. (B) Fluorescence emission spectrum of **HJTA** (1  $\mu$ M) at  
59  
60

different pH (7.67 – 3.17) in an aqueous solution containing 1% (v/v) DMSO, ( $\lambda_{\text{ex}} = 445 \text{ nm}$ ). (C) Absorbance-pH titration profiles of **HJTA** at absorption wavelength of 445 nm. (D) Fluorescence intensity-pH titration profiles of **HJTA** at emission wavelength of 490 nm. Insert: fluorescence images of **HJTA** (5  $\mu\text{M}$ ) at pH = 7.4 and pH = 4.0 under 365 nm UV light.

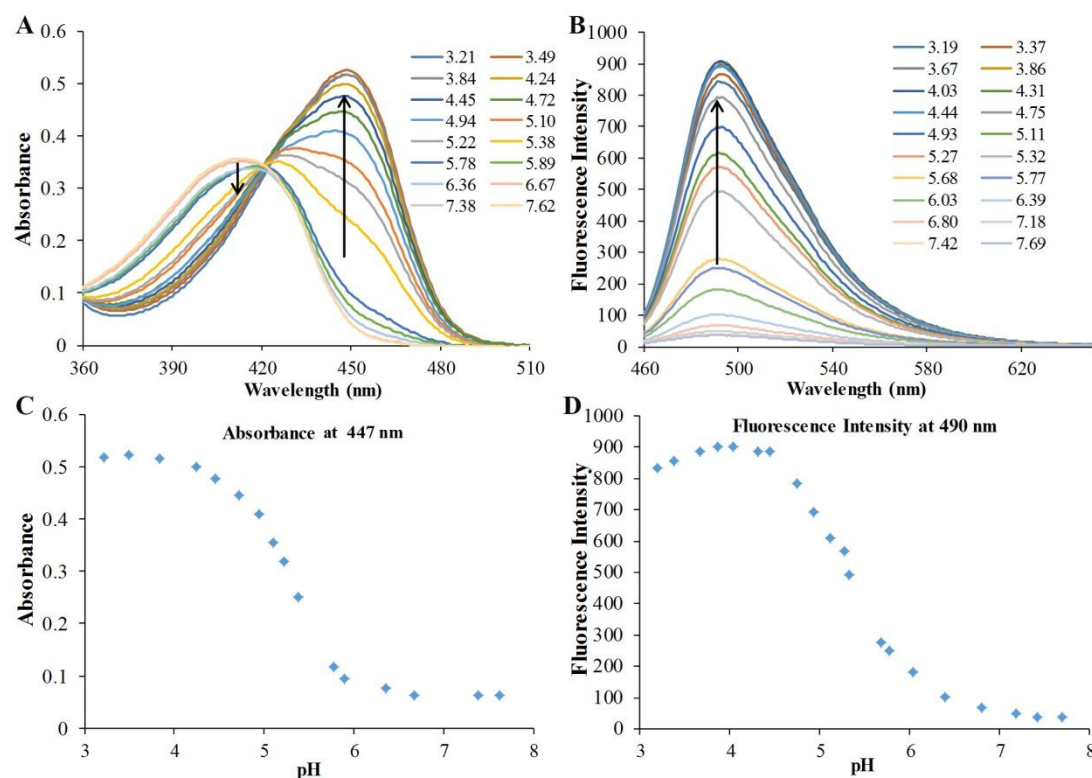
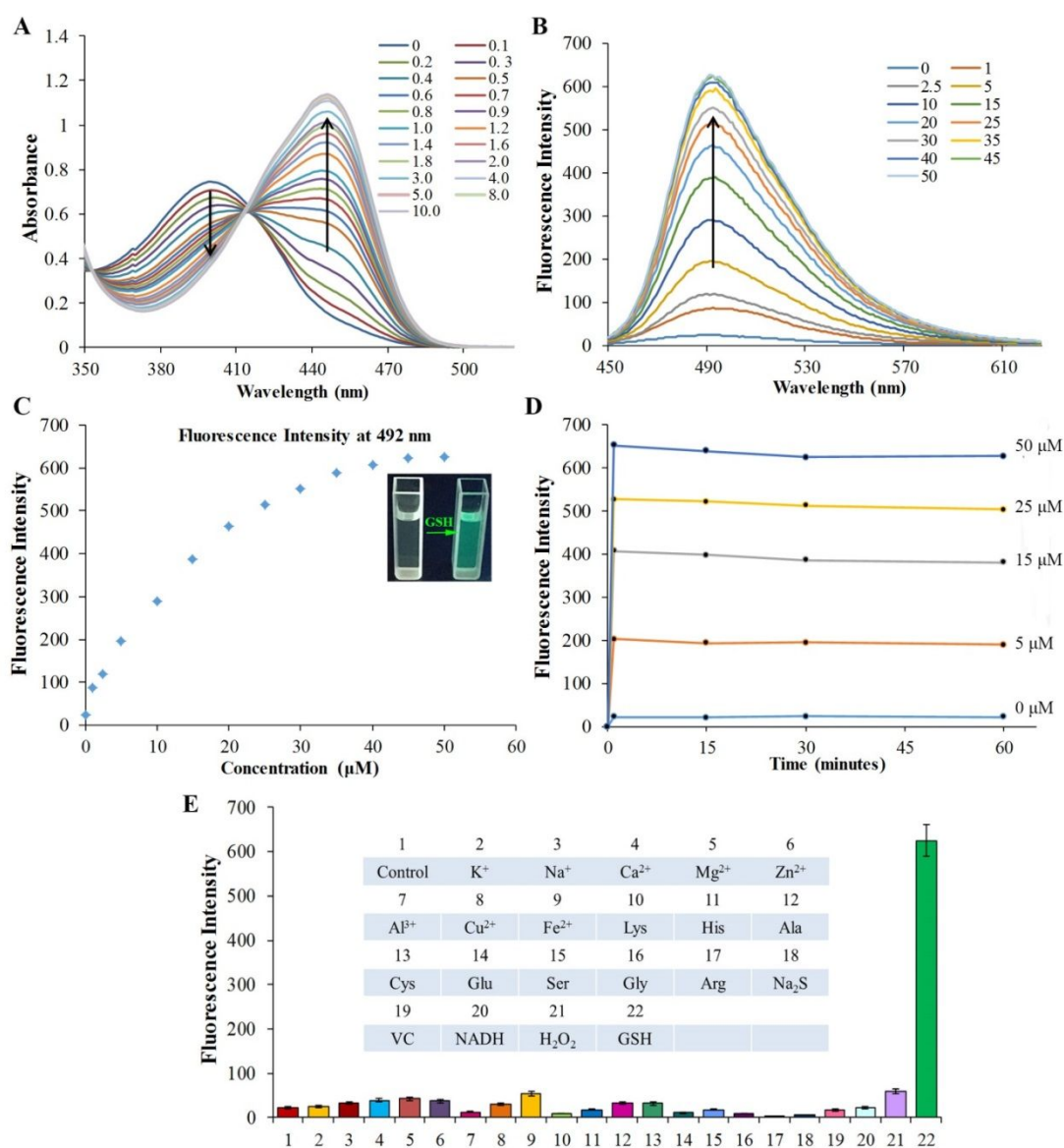


**Figure 3.** (A) Absorption spectra of **HJT B** (100  $\mu\text{M}$ ) at different pH (7.62 - 3.21) in an aqueous solution containing 1% (v/v) DMSO. (B) Fluorescence emission spectrum of **HJT B** (1  $\mu\text{M}$ ) at different pH (7.69 – 3.19) in an aqueous solution containing 1% (v/v) DMSO, ( $\lambda_{\text{ex}} = 447 \text{ nm}$ ). (C) Absorbance-pH titration profiles of **HJT B** at absorption wavelength of 447 nm. (D) Fluorescence intensity-pH titration profiles of **HJT B** at emission wavelength of 490 nm.

### 2.3 GSH response of **6**, **HJTA** and **HJT B**

The responses of **HJTA** and **HJT B**, along with **6**, to GSH were measured in aqueous solutions containing 1% DMSO (v/v) with the enzyme GST $\pi$  at 37  $^{\circ}\text{C}$ . As shown in Figure S4, no detectable change in fluorescence was observed with **6** after addition of GSH (0 – 360  $\mu\text{M}$ ). However, the absorption of the **HJTA** (100  $\mu\text{M}$ ) solution rapidly increased to above 440 nm (Figure 4A). Further, the solution exhibited a marked enhancement of fluorescence intensity at

around 492 nm in a dose-dependent manner and showed obvious green fluorescence that could be clearly observed under 365 nm ultraviolet lamp (Figure 4C). The fluorescent signal of **HJTA** after addition of GSH was stable and lasted over 1 h at 37 °C (Figure 4D). These data support that **HJTA** can serve as a prominent GSH responsive fluorescent on-off switch. From the fluorescence spectrum in Figure S5b, it can be seen that both **HJTA** and **HJTB** displayed a typical fluorescence enhancement in the range of 450-600 nm. Interestingly, while **HJTB** has two GSH/GST $\pi$  reactive sub-units and **HJTA** only has one such unit, **HJTB** had weaker fluorescence than **HJTA** (Figure 4B vs. Figure S5B). Further, the time of fluorescence intensity reaching a plateau (1.5h) after the addition of GSH was also longer for **HJTB** than that **HJTA**, suggesting that **HJTB** is less sensitive for the rapid detection of GSH (Figure S5D).



1  
2  
3 **Figure 4.** (A) Absorption spectra of **HJTA** (100  $\mu\text{M}$ ) in the presence of varying amount of GSH  
4 (0 ~ 10 equiv) with cat. GST $\pi$  in an aqueous solution containing 1% (v/v) DMSO. The spectra  
5 were recorded after incubation at 37  $^{\circ}\text{C}$  for 0.5 h. (B) Fluorescence emission spectrum of **HJTA**  
6 (1  $\mu\text{M}$ ) at 492 nm as a function of varying concentrations of GSH with cat. GST $\pi$  in an aqueous  
7 solution containing 1% DMSO (v/v), ( $\lambda_{\text{ex}} = 445 \text{ nm}$ ). (C) Fluorescence intensity-concentration  
8 (GSH) titration profiles of **HJTA** at emission wavelength of 492 nm. Insert: fluorescence images  
9 of **HJTA** (5  $\mu\text{M}$ ) without and with the presence of GSH (50.0  $\mu\text{M}$ ) under 365 nm UV light. (D)  
10 GSH concentration (0, 5, 15, 25, 50  $\mu\text{M}$ )-dependent fluorescence activation rates of **HJTA** (1  $\mu\text{M}$ ).  
11 (E) Fluorescence response of **HJTA** (1  $\mu\text{M}$ ) with cat. GST $\pi$  after treatment with various  
12 biological analytes: 1 mM of ( $\text{K}^+$ ,  $\text{Na}^+$ ,  $\text{Ca}^{2+}$ ,  $\text{Mg}^{2+}$ ,  $\text{Zn}^{2+}$ ,  $\text{Al}^{3+}$ ,  $\text{Cu}^{2+}$ ,  $\text{Fe}^{2+}$ ); 100  $\mu\text{M}$  of (GSH, lys,  
13 his, ala, cys, glu, ser, gly, arg, VC,  $\text{Na}_2\text{S}$ ); and 50  $\mu\text{M}$  of NADH and  $\text{H}_2\text{O}_2$ . Bars represent  
14 comparative fluorescence changes at 492 nm,  $\lambda_{\text{ex}} = 440 \text{ nm}$ .  
15  
16  
17  
18  
19  
20  
21  
22  
23  
24  
25  
26  
27  
28

29 The observed fluorescence change is likely the result of the formation of adduct **5**, which  
30 formed via the reaction of GSH with **HJTA** or **HJTB** (Figure 1). Thus, the aqueous solution of  
31 the more GSH responsive **HJTA** and GSH were analyzed using HRMS. A mass peak of 809  
32 (exact mass calcd for  $\text{M} + \text{H}^+$ , 809.2825) was generated (Figure S14), confirming **5** formation.  
33 This result indicates that GSH has the ability to covalently bind to the enone functionality of  
34 **HJTA**.  
35  
36  
37  
38  
39  
40  
41  
42

43 To verify the selectivity of **HJTA** for GST $\pi$  against other GST enzymes, the percentages of **6**  
44 release were analyzed by HPLC after incubation of **HJTA** (40  $\mu\text{M}$ ) in the presence of GSH (0.8  
45 mM) and GST $\pi$  or GST $\alpha$  (0.03  $\mu\text{g}/\text{ml}$ ). Enzymatic reactions of **HJTA** with GST $\pi$ , but not GST $\alpha$   
46 (Figure S17), were observed under the same conditions, confirming the selectivity of **HJTA** for  
47 GST $\pi$ .  
48  
49  
50  
51  
52  
53  
54  
55

#### 56 2.4 Selective response of **HJTA** to GSH

57  
58

59 To confirm that the response of **HJTA** toward GSH/GST $\pi$  is selective, a variety of  
60

1  
2  
3  
4 physiological environment relevant species, including inorganic metal ions, amino acids,  
5  
6 reductants and oxidants, were analyzed at pH 7.4. As shown in Figure 4E, inorganic salts ( $K^+$ ,  $Na^+$ ,  
7  
8  $Ca^{2+}$ ,  $Mg^{2+}$ ,  $Zn^{2+}$ ,  $Al^{3+}$ ,  $Cu^{2+}$ ,  $Fe^{2+}$ ), amino acids (lysine, histidine, alanine, cysteine, glutamic acid,  
9  
10 serine, glycine, arginine), reductants (Vitamin C,  $Na_2S$ ),  $H_2O_2$ , and NADH did not cause any  
11  
12 apparent change of the fluorescence intensity. These results demonstrate that **HJTA** is highly  
13  
14 selective in specific response to GSH and pH.  
15  
16  
17  
18  
19  
20  
21

## 22 **2.5 Cellular uptake of HJTA**

23  
24 The intracellular fluorescence of **HJTA** was subsequently evaluated in cancer HT29 cells and  
25  
26 normal CCD841 cells to evaluate its cellular uptake. The time course of **HJTA** ( $1.0 \mu M$ ) cellular  
27  
28 uptake was determined by quantifying intracellular fluorescent intensity of HT29 cells and  
29  
30 CCD841 cells within 60 min (Figure S6). The confocal fluorescence images indicate that the  
31  
32 uptake of **HJTA** was rapid and increased comparably for HT29 cells within the first 10 min  
33  
34 (Figure S6A), while it was minimal for CCD841 cells during the same time frame. In addition, the  
35  
36 final fluorescence intensity in HT29 cells was significantly higher than that of CCD841 cells,  
37  
38 suggesting more efficient accumulation of **HJTA** in HT29 cells. This is likely the result of the  
39  
40 targeting ability of **HJTA** for the overexpressed GSH and/or the lower pH in lysosomes in these  
41  
42 cancer cells.<sup>21,22</sup>  
43  
44  
45

46 We then treated both HT29 and CCD841 cells with **HJTA** ( $1.0 \mu M$ ) and co-incubated with a  
47  
48 commercial lysosomal probe (Lyso-Tracker), which labels and tracks acidic organelles in live  
49  
50 cells, for 60 min to examine intracellular fluorescence activation. For CCD841 cells which do not  
51  
52 overexpress GSH, the green emission upon treatment with **HJTA** was weak and little overlapped  
53  
54 with the red signal in the lysosomes (Figure 5B). However, the green emission was significantly  
55  
56 stronger for the GSH overexpressed HT29 cells than that of CCD841 cells upon treatment with  
57  
58 **HJTA**. Confocal images showed that the green fluorescent signal largely overlapped with the red  
59  
60 fluorescent signals from Lyso-Tracker (Figure 5A), consistent with its sensitivity to acidic

environments and GSH. These studies clearly demonstrate that **HJTA** can target and monitor cancer cells extensively overexpressing GSH and having lower pH with good sensitivity as designed.

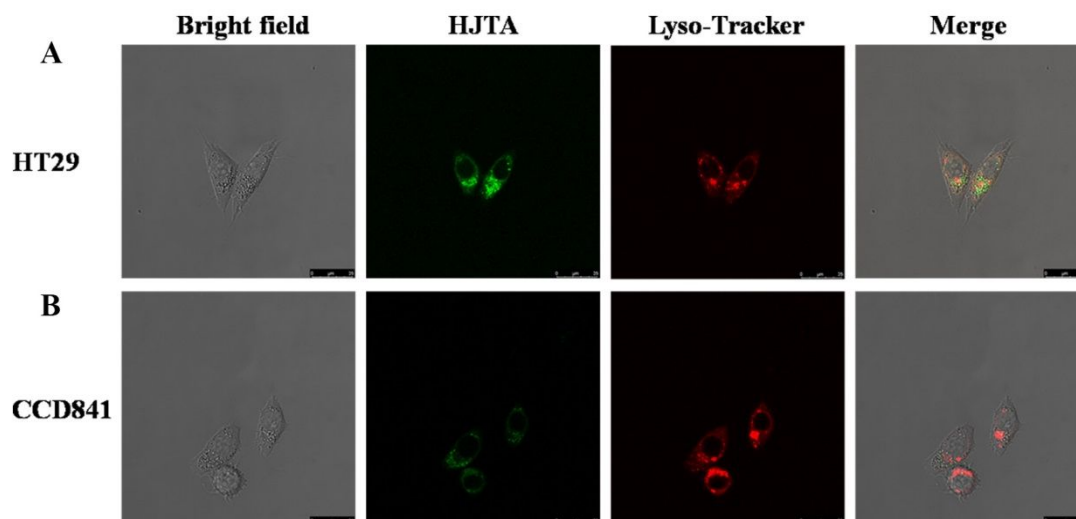


**Figure 5.** Intracellular fluorescent activation of **HJTA** and cell viabilities. (A) Confocal microscopy images of HT29 cells treated with **HJTA** and Lyso-Tracker. (B) Confocal microscopy images of CCD841 cells incubated with **HJTA** and Lyso-Tracker. Scale bar for all images = 25  $\mu\text{m}$ . For **HJTA** (green channel), an excitation wavelength of  $\lambda_{\text{ex}} = 440 \text{ nm}$  was used. For Lyso-Tracker (red channel):  $\lambda_{\text{ex}} = 561 \text{ nm}$ .

## 2.6 In vitro antitumor activities and selectivity

Now that we have demonstrated the fluorescent and visualizing capability of **HJTA** in vitro, we next determined the antiproliferative effect of **HJTA** and **HJTB** on HT29, HepG2 and 9L-2 cells by MTT assay. HT29, HepG2 cells as GST $\pi$  activity “+” and 9L-2 cells<sup>34</sup> as GST $\pi$  activity “-” were employed to examine the antiproliferative selectivity of **HJTA** and **HJTB** for GST $\pi$ -overexpressed cancer cells. Compound **6**, COMC-6, and harmine (a naturally occurring  $\beta$ -carboline) were used as the positive controls. Both **HJTA** and **HJTB** exhibited prominent inhibitory activities against three tumor cell lines with IC<sub>50</sub> values on single-digit micromole levels. Furthermore, the inhibitory potencies of **HJTA** and **HJTB** on HT29 and HepG2 cells with GST $\pi$  activity as “+” (IC<sub>50</sub> values of 0.92-2.69  $\mu\text{M}$ ) were greater than 9L-2 cells with GST $\pi$  activity as “-” (IC<sub>50</sub> values of 4.32-4.85  $\mu\text{M}$ ), indicating a positive association between GST $\pi$

activity and the antiproliferative activity of **HJTA** and **HJTB**. Noticeably, **HJTA**, the more potent compound, exerted significant anticancer activities with  $IC_{50}$  value of 0.92  $\mu$ M against colonic cancer cells, 5-fold better than COMC-6 ( $IC_{50}$  = 4.37  $\mu$ M), 14-fold better than  $\beta$ -carboline moiety **6** ( $IC_{50}$  = 13.5  $\mu$ M), and even 3-fold better than the combination of COMC-6 and **6** ( $IC_{50}$  = 2.81  $\mu$ M). **HJTA** also exerted over 3-fold weaker toxicity on intestinal normal cells CCD841 than COMC-6, demonstrating a greater therapeutic window for **HJTA** than COMC-6 (Table 1). **HJTA** had greater anti-tumor activities than **HJTB** against all 3 cell lines. This result is consistent with their GSH-responsiveness (**HJTA** > **HJTB**), likely leading to incomplete degradation of **HJTB** by GSH/GST $\pi$  and thus less amount of generated reactive species (compound **3**). Based on these considerations, **HJTA** was selected in subsequent investigations.

**Table 1.** The  $IC_{50}$  ( $\mu$ M) of **HJTA** and **HJTB** against three cancer cell lines and one intestinal normal cell line <sup>a</sup>

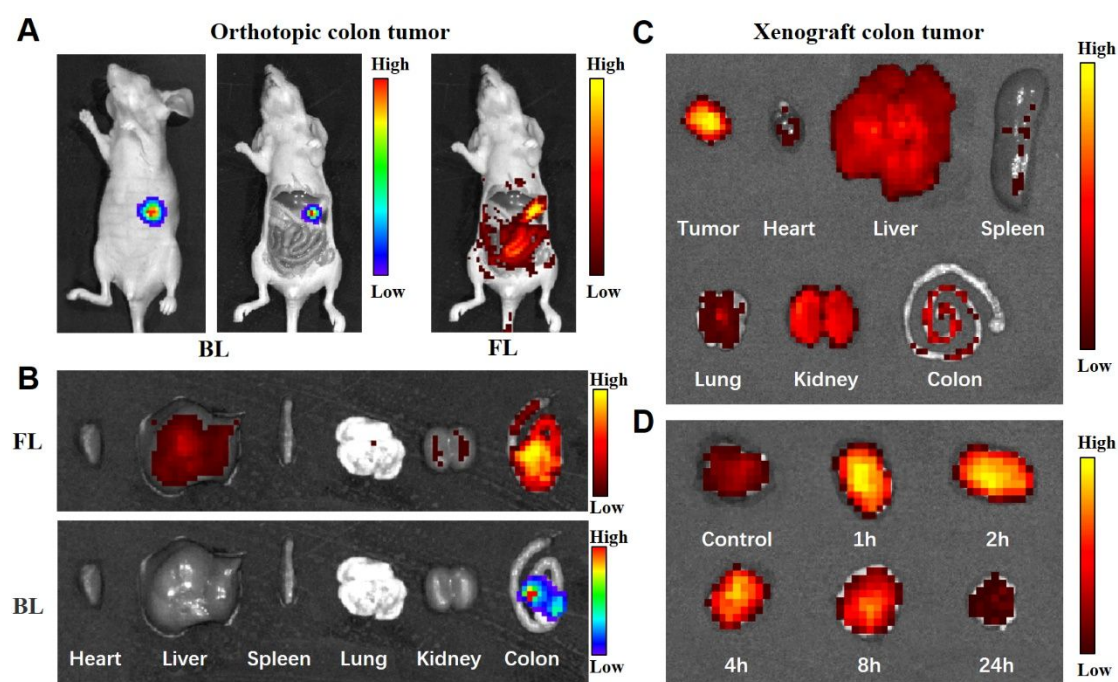
Compound	$IC_{50}$ ( $\mu$ M) <sup>a</sup>			
	HT29 <sup>b</sup>	HepG2	9L-2 <sup>c</sup>	CCD841
COMC-6	4.37 $\pm$ 0.39	5.93 $\pm$ 0.67	7.79 $\pm$ 0.48	7.83 $\pm$ 0.55
<b>6</b>	13.5 $\pm$ 0.96	17.1 $\pm$ 1.28	ND	ND
COMC-6 + <b>6</b>	2.81 $\pm$ 0.43	4.09 $\pm$ 0.56	ND	ND
<b>HJTA</b>	0.92 $\pm$ 0.11	1.57 $\pm$ 0.20	4.32 $\pm$ 0.36	23.4 $\pm$ 2.72
<b>HJTB</b>	1.45 $\pm$ 0.24	2.69 $\pm$ 0.31	4.85 $\pm$ 0.61	28.1 $\pm$ 3.11
Harmine	41.8 $\pm$ 3.75	49.6 $\pm$ 3.89	47.8 $\pm$ 5.24	>50

<sup>a</sup>The  $IC_{50}$  data (means  $\pm$  SD) were from three separated experiments. <sup>b</sup>GST $\pi$  activity as “+”.

<sup>c</sup>GST $\pi$  activity as “-”.

## 2.7 Imaging-guided surgery of colon tumors

1  
2  
3  
4 Considering its encouraging in vitro results in simultaneously targeting pH and GSH, **HJTA**  
5  
6 was investigated for its ability to visualize tumor tissues and to guide resection of orthotopic  
7  
8 HT29 colon tumors. Thus, luciferase-marked HT29 (HT29/Luc) cells were injected into the upper  
9  
10 part of the colons to construct an orthotopic colon tumor model in the mice. Two weeks later,  
11  
12 clear bioluminescence (BL) was seen, indicating successful formation of HT29/Luc tumors in the  
13  
14 colon of mice. Upon intravenous administration of **HJTA**, bright fluorescence was observed in the  
15  
16 colon position, overlapping well with the BL imaging position (Figure 6A). To further validate the  
17  
18 specificity of **HJTA** for tumor tissues versus normal tissues, the mice were sacrificed, and the  
19  
20 orthotopic colon tumor and main organs were analyzed by BL and fluorescence imaging. The  
21  
22 fluorescent signal was significantly greater in the colon tumor than the other organs, and also  
23  
24 overlapped well with the BL imaging (Figure 6B). These results confirm that **HJTA**, as a  
25  
26 promising molecular imaging tool, is capable of locating orthotopic colon tumor tissues in living  
27  
28 systems via noninvasive fluorescence imaging, which could assist fluorescence-guided surgical  
29  
30 removal of colon tumor.  
31  
32  
33  
34  
35  
36  
37  
38  
39



1  
2  
3 **Figure 6.** Fluorescence-guided location of orthotopic colon tumors. (A) Full-body  
4 bioluminescence (BL, left) and fluorescence (FL, right) imaging of orthotopic HT29/Luc colon  
5 tumor in intraoperative mice after 2 h post intravenous injection with **HJTA** (40 mg/kg). (B) *Ex*  
6 *vivo* bioluminescence (up) and fluorescence (down) imaging of main organs removed from  
7 orthotopic HT29/Luc colon tumor mice model ( $\lambda_{ex/em} = 430/490$  nm). (C) *Ex vivo* fluorescence  
8 imaging of tumor and main organs removed from HT29 colon xenograft mice model after 2 h post  
9 intravenous injection with **HJTA** (40 mg/kg). (D) *Ex vivo* fluorescence imaging of tumor  
10 extirpated from subcutaneous tumor mice model at various time points post intravenously injected  
11 with **HJTA** (40 mg/kg).  
12  
13  
14  
15  
16  
17  
18  
19  
20  
21  
22  
23  
24

25 We have clearly demonstrated that **HJTA** successfully penetrated into cells/tissues and  
26 selectively illuminated tumors as designed. Theranostic agents are also required to have good  
27 stability and be retained at the targeted tissue for sufficiently long. Therefore, the fluorescence  
28 biodistribution of **HJTA** was then investigated in tumor-bearing mice using *ex-vivo* imaging. Two  
29 hours after intravenous injection of **HJTA** (40 mg/kg), the mice were sacrificed and the tumor and  
30 major organs including the heart, lung, liver, kidney, colon, and spleen, were examined. As clearly  
31 shown in Figure 6C, the fluorescent signal was significantly greater in the tumor than the major  
32 organs (Figure 6C). Strong fluorescent signal was observed in tumors 1 hour after injection and  
33 lasted for over 7 hours (Figure 6D). These results confirmed the efficient retention of **HJTA** in the  
34 tumor with promising selectivity and visualization *in vivo*.  
35  
36  
37  
38  
39  
40  
41  
42  
43  
44  
45  
46  
47  
48  
49  
50  
51  
52

### 53 **2.8 *In vivo* anti-cancer efficacy of HJTA**

54  
55 To assess the *in vivo* safety and efficacy profile of **HJTA**, ICR mice were intraperitoneally  
56 injected with different doses of **HJTA**. The percentage of survival was monitored for 14 days after  
57  
58  
59  
60

1  
2  
3  
4 administration. As depicted in Table 2, at the highest dose of **HJTA** (585.9 mg/kg), only one  
5  
6 mouse treated survived. In contrast, no death or abnormality in body weight, drinking, eating, or  
7  
8 activity was found after administration with **HJTA** at the lowest dose (240 mg/kg). Accordingly,  
9  
10 the acute toxicity of **HJTA** was analyzed and the median lethal dose (LD<sub>50</sub>) value was determined  
11  
12 to be 475 mg/kg.  
13  
14  
15  
16  
17  
18  
19

20 **Table 2.** Acute toxicity of **HJTA** in mice

Dose (mg/kg)	Number of mice	Number of dead mice							Total death	Survival (%) on day 14
		1h	4h	1d	2d	3d	4d	5-14d		
585.9	10	0	0	3	2	2	1	1	9	10
468.8	10	0	0	2	2	1	1	0	6	40
375.0	10	0	0	0	1	0	1	0	2	80
300.0	10	0	0	0	0	0	0	0	0	100
240.0	10	0	0	0	0	0	0	0	0	100

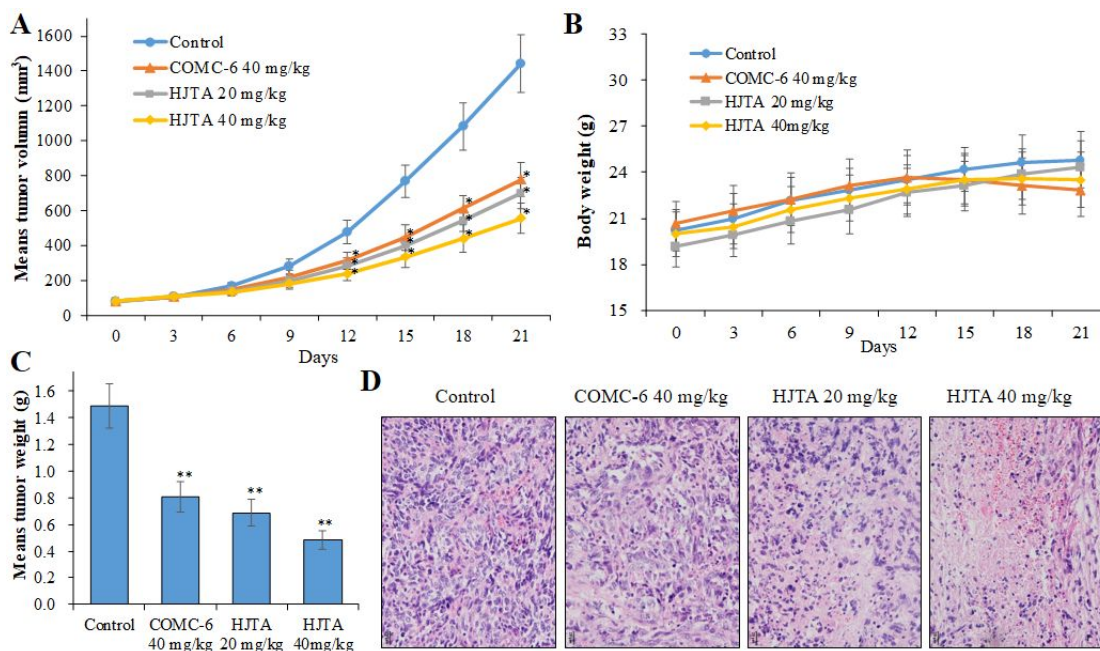


**Figure 7.** The antitumor effect of **HJTA** on HT29 xenograft in nude mice. (A) After establishing xenograft mice model, tumor volume changes in tumor-bearing mice administrated with saline control, COMC-6, or **HJTA** were surveyed during 21 days. \* $P < 0.05$  vs control group. (B) Body weight was monitored every three days. (C) Tumor weight was measured at the end of the treatment. \*\* $P < 0.01$  vs control group. (D) Histological sections of tumors stained with H&E. Scale bar for all images = 100  $\mu\text{m}$ .

In order to assess the *in vivo* antitumor efficacy of **HJTA**, four BALB/c nude mice groups were subcutaneously injected with HT29 cells. After establishing xenograft mice model, these tumor-bearing mice were intraperitoneally injected with saline, **HJTA**, and COMC-6 every day for 21 days, respectively. The body mass and tumor size of nude mice were surveyed every three days during the 21 days. As shown in Figure 7A, A sustainable tumor growth was observed with the saline treated group. In contrast, the intraperitoneal treatment of **HJTA** apparently diminished the volumes of xenograft tumors. **HJTA** also led to greater tumor reduction than COMC-6 at the

1  
2  
3  
4 end of the treatment period. However, no significant statistical difference in body mass changes  
5  
6 between the **HJTA**-treated groups and vehicle groups was observed (Figure 7B). The tumor  
7  
8 weight ( $0.48 \pm 0.07$  g) in mice dosed by **HJTA** at 40 mg/kg was diminished by 67.7% (w/w)  
9  
10 compared to the saline groups ( $1.49 \pm 0.27$  g), and was lower than the tumor weight ( $0.81 \pm 0.12$   
11  
12 g) of COMC-6 groups at 40 mg/kg (Figure 7C). Together, these data clearly confirm that **HJTA**  
13  
14  
15 possessed remarkable inhibitory potency of the tumor growth in vivo.  
16  
17  
18  
19  
20

## 21 **2.9 Anticancer Mechanism Studies**

22  
23 Apoptosis is one of the critical mechanisms of cell death following exposure to  
24  
25 chemotherapy.<sup>35,36</sup> Since **HJTA** exerted significant and selective tumor cell inhibitory activities, it  
26  
27 was evaluated for its potency to promote cancer cell apoptosis. Therefore, HT29 cells were  
28  
29 inoculated with COMC-6, harmine, or **HJTA** for 72 h, and the apoptotic cell percentages were  
30  
31 analyzed through FITC-Annexin V/PI staining and flow cytometry. As depicted in Figure 8, cells  
32  
33 incubated with increasing concentrations of **HJTA** exhibited potent apoptotic rates (36.8% for 1.0  
34  
35  $\mu\text{M}$  and 52.3% for 2.5  $\mu\text{M}$ ) in annexin V + HT29 cells, which were significantly better than the  
36  
37 harmine (20.9% for 10  $\mu\text{M}$ ) and COMC-6 (28.8% for 2.5  $\mu\text{M}$ ) groups. Accordingly, **HJTA**  
38  
39 exerted HT29 cell apoptosis induction with greater efficacy than harmine and COMC-6.  
40  
41  
42

43 To further verify the apoptosis induction effect of **HJTA**, expressions of apoptosis-related  
44  
45 proteins, including Bcl-2, Bax, and the cleavage of caspase-3 and PARP (apoptotic key markers)  
46  
47 were detected.<sup>37,38</sup> HT29 cells were incubated with vehicle, **HJTA**, COMC-6, or harmine,  
48  
49 respectively, for 72 h and the cells were lysed and subjected to analysis in Western blot (WB).  
50  
51 According to Figure 8A, **HJTA** dose-dependently augmented the pro-apoptotic Bax levels but  
52  
53 diminished the anti-apoptotic Bcl-2 levels. In addition, **HJTA** also resulted in the accumulation of  
54  
55 cleaved-PARP and caspase-3, both more significantly than harmine- or COMC-6-treated group.  
56  
57 Overall, these analyses suggested that **HJTA** induced apoptosis by the regulation of apoptotic  
58  
59 related proteins in HT29 cells.  
60

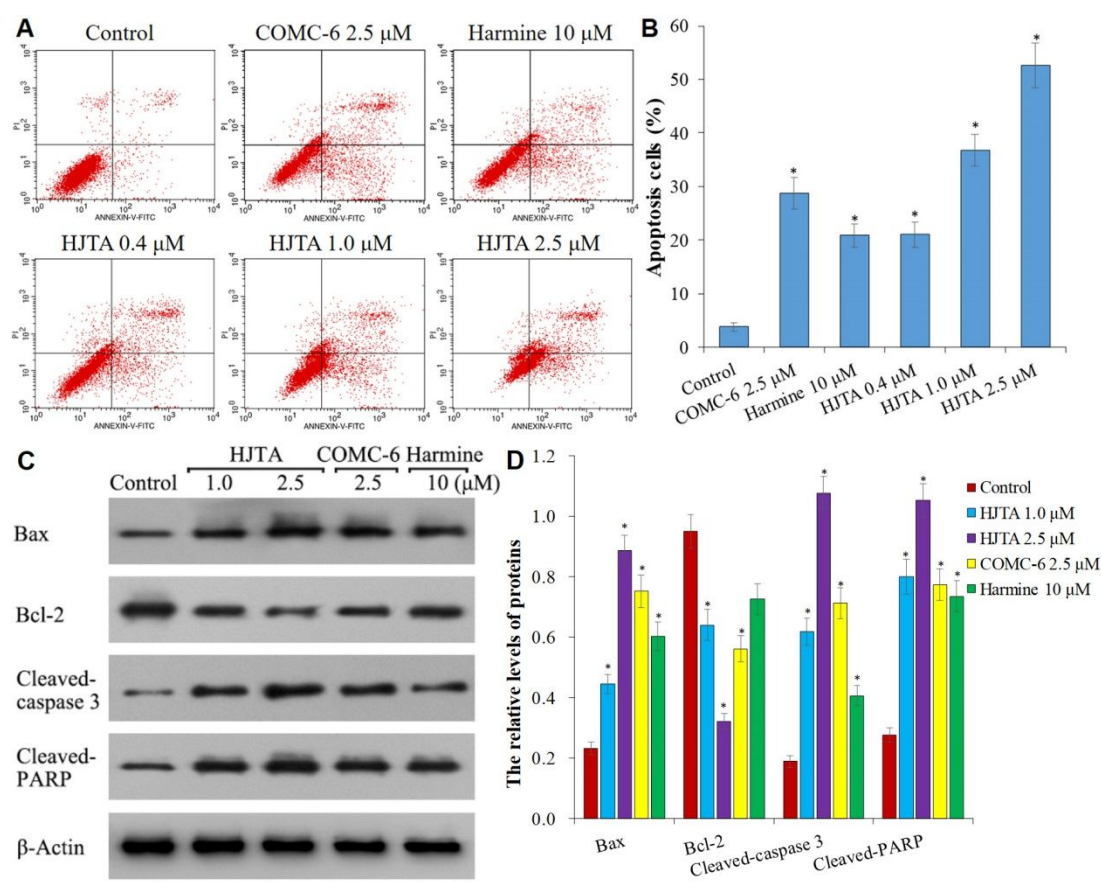


**Figure 8.** Compound **HJTA** induced HT29 cell apoptosis. (A) HT29 cells were treated with the different concentrations of **HJTA**, COMC-6, or harmine for 72 h, and stained with FITC-Annexin V and PI through flow cytometry analysis. (B) The apoptotic rates were quantitatively analyzed, and data (means  $\pm$  SD) were collected from three separated experiments.  $*P < 0.01$  vs control. (C) The levels of apoptosis related proteins in HT29 cells upon with **HJTA**, COMC-6, or harmine in WB assay. (D) The relative levels of each apoptosis protein were quantitatively analyzed compared to the internal reference  $\beta$ -actin, and the related data (means  $\pm$  SD) were from three independent assays.  $*P < 0.01$  vs vehicle control.

Autophagy, a natural and well-conserved cellular catabolic process regulating the cell in disassembling dysfunctional or unnecessary components, is regarded as an effective strategy to enhance antineoplastic effects of chemotherapeutic agents and improve their therapeutic outcome in cancer patients.<sup>39-41</sup> The potential and mechanism of **HJTA** inducing autophagy were assessed by testing the levels of key autophagic related proteins. The conversion of LC3-I to LC3-II is a

crucial point in autophagy. Thus, the changes of autophagic markers LC3-I/-II, Beclin-1, and p62 proteins in response to **HJTA** treatment were examined in HT29 cells. As depicted in Figure 9, the levels of LC3-II and Beclin-1 proteins dose-dependently increased, while the expression of p62 was downregulated upon treatment with **HJTA** of different concentrations. Noticeably, the LC3-II/LC3-I ratio and the levels of LC3-II in **HJTA**-treated groups were higher than both the harmine and COMC-6-treated groups (Figure 9B). These results indicated that **HJTA** could markedly lead to an autophagic induction in HT29 cells.

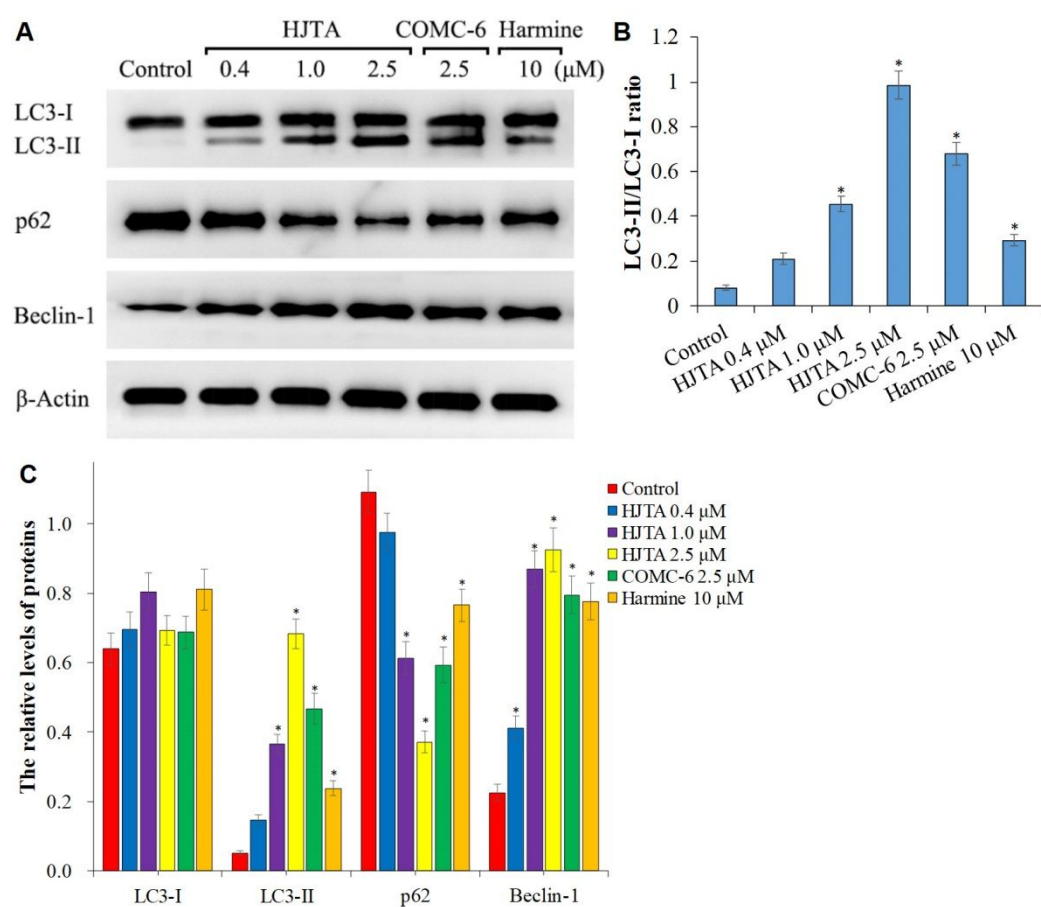


**Figure 9.** Compound **HJTA** promoted autophagic induction. (A) Autophagy-associated proteins (LC3-I/-II, p62, and beclin-1) were detected by WB assay in HT29 cells treated with vehicle, **HJTA**, COMC-6, or harmine. (B) The LC3-II/LC3-I ratio was quantitatively analyzed. (C) The comparative levels of LC3-I/-II, p62, and beclin-1 to the internal reference  $\beta$ -actin were quantitatively analyzed. The related data (means  $\pm$  SD) were from three independent assays. \* $P$  < 0.01 vs respective vehicle control.

### 3. Conclusions

In summary, we have for the first time developed excellent theranostics **HJTA** and **HJTB** as intraoperative fluorescence diagnostic and chemotherapeutic agents for colonic cancer *in vivo*. The results showed that **HJTA** and **HJTB** not only displayed dual pH/GSH responsive fluorescence features, but also selectively inhibited tumor cell proliferation. Importantly, **HJTA** selectively and precisely illuminated cancer cells and tumor tissues, and accurately located orthotopic colonic tumor foci through the blood circulation system, providing an image-guided tool for surgical resection of tumor tissues in intraoperative mice. Meanwhile, the positive tumor inhibition of **HJTA** and its significant apoptotic and autophagic induction may provide simultaneous chemotherapy, in addition to real-time fluorescence diagnosis, to prevent invasion and metastasis of cancer cells. Thus, we believe that this theranostic probe designed for intraoperatively monitoring of TME combined with selective antitumor activity would add a much needed tool to the current cancer diagnosis strategies and may improve patient prognosis and broaden the impact of small multifunctional molecules in enzyme mapping, tumor theranostic and image-guided surgery.

### 4. MATERIALS AND METHODS

#### 4.1 Materials

All chemical reagents were purchased from Aladdin or Sigma-Aldrich and used without further purifications. All reactions were carried out under air atmosphere if no additional indication.  $^1\text{H}$  and  $^{13}\text{C}$  NMR spectra were obtained on a Bruker AV 400 M spectrometer with tetramethylsilane as the internal standard. Mass spectra was recorded on a Mariner mass spectrometer (ESI). UV-visible spectra were obtained on a spectrometer (UV1800PC, Jinghua, China). Fluorescence spectroscopic studies were performed on a fluorescence spectrophotometer (RF-5301PC, Shimadzu, Japan). HRMS data were recorded on a JMS-SX102A (FAB) or LC/MSD TOF. Compounds **7**, **10**, **11** were commercially available. Compounds **6** and **12-16** were synthesized according literatures.<sup>42</sup> Purities of target compounds reached at least >95% pure by analytical HPLC (Figure S15, S16).

## 4.2 Synthesis of HJTA and HJTB

### 2-Hydroxymethyl-2-cyclohexen-1-one (**8**)

To a solution of 2-cyclohexen-1-one **7** (4.8 g, 50 mmol) in 30 mL THF were added formaldehyde (4.2 g, 60 mmol) and DMAP (0.63 g, 5 mmol) and stirred for 18 hours. After TLC monitored the total consumption of starting material, the reaction mixture was quenched with water 120 mL, followed by extracted with CH<sub>2</sub>Cl<sub>2</sub> (40 ml × 3). The combined organic extracts were dried over anhydrous Na<sub>2</sub>SO<sub>4</sub>, filtered, concentrated in vacuo, and finally purified by flash column chromatography to give the product **8** as a yellow oil (5.4 g, 85.7%). Spectral data are in agreement with literature values.<sup>43</sup> <sup>1</sup>H NMR (DMSO-*d*<sub>6</sub>, 400 MHz): δ 6.95 (s, 1H), 4.77 (t, 1H, *J* = 5.5 Hz), 4.12 – 3.94 (m, 2H), 2.00 – 1.78 (m, 4H), 2.00 – 1.78 (m, 2H).

(6-Oxocyclohex-1-en-1-yl)methyl (1-(3,4,5-trimethoxyphenyl)-9H-pyrido[3,4-*b*]indol-3-yl) carbamate (**HJTA**) and di(6-oxocyclohex-1-en-1-yl)methyl(1-(3,4,5-trimethoxy phenyl)-9H-pyrido[3,4-*b*]indol-3-yl)carbamate (**HJTB**)

Compound **8** (252 mg, 2.0 mmol) and 4-nitrophenyl carbonochloridate (605 mg, 3.0 mmol) were dissolved in 15 mL dry CH<sub>2</sub>Cl<sub>2</sub> cooled to 0 °C. DIPEA (505 mg, 5.0 mmol) was added and the mixture was stirred for 2 h at 0 °C, at which point reaction was completed. The mixture was diluted with CH<sub>2</sub>Cl<sub>2</sub> (40 mL), washed with saturated aqueous NaHCO<sub>3</sub> (15 mL), and brine. Then organic layer was dried with Na<sub>2</sub>SO<sub>4</sub> and concentrated under reduced pressure. The crude product was purified by silica gel column chromatography using Petroleum ether/EtOAc (8:1, v : v) as eluent to afford **9** as a yellow solid (410 mg, 70.4%).

Compound **9** (436 mg, 1.5 mmol) and compound **6** (349 mg, 1.0 mmol) were dissolved in 5 mL dry CH<sub>2</sub>Cl<sub>2</sub> at 0 °C, and DIPEA (505 mg, 5.0 mmol) was added to the above solution and the

1  
2  
3  
4 mixture stirred at room temperature for 4 hours. The solvent was evaporated under vacuum. The  
5  
6 crude solid was purified by a silica gel column using Petroleum ether/EtOAc (2:1, v : v) as eluent  
7  
8  
9 to obtain **HJTA** (202 mg, 40.3%) and **HJTB** (140 mg, 27.9%).

10  
11 Analytical data for **HJTA**:  $^1\text{H}$  NMR (DMSO- $d_6$ , 400 MHz):  $\delta$  10.83 (s, 1H), 8.07 (d, 1H,  $J$  =  
12  
13 7.6 Hz), 7.49 – 7.45 (m, 2H), 7.21 (s, 2H), 7.13 – 7.09 (m, 2H), 6.99 (s, 1H), 6.13 (s, 1H), 4.11 –  
14  
15 4.10 (m, 2H), 3.91 (s, 6H), 3.76 (s, 3H), 2.43 – 2.36 (m, 2H), 2.34 – 2.33 (m, 2H), 1.95 – 1.87 (m,  
16  
17 2H).  $^{13}\text{C}$  NMR (DMSO- $d_6$ , 101 MHz):  $\delta$  199.3, 153.4, 152.5, 145.8, 143.0, 138.2, 137.0, 128.4,  
18  
19 127.9, 126.6, 122.0, 121.3, 118.8, 116.3, 112.5, 106.1, 95.6, 60.5, 56.3, 38.6, 25.7, 23.2. HRMS:  
20  
21 (ESI,  $m/z$ ) Calcd for  $\text{C}_{28}\text{H}_{27}\text{N}_3\text{NaO}_6$   $[\text{M}+\text{Na}]^+$ : 524.1792, found 524.1785.

22  
23 Analytical data for **HJTB**:  $^1\text{H}$  NMR (DMSO- $d_6$ , 400 MHz):  $\delta$  10.89 (s, 1H), 8.15 (d,  $J$  = 8.1 Hz,  
24  
25 1H), 7.50 – 7.43 (m, 2H), 7.23 (s, 2H), 7.18 (s, 1H), 7.13 – 7.09 (m, 1H), 6.73 (s, 2H), 4.35 (s, 4H),  
26  
27 3.89 (s, 6H), 3.76 (s, 3H), 2.42 – 2.37 (m, 4H), 2.31 (s, 4H), 1.92 – 1.90 (m, 4H).  $^{13}\text{C}$  NMR  
28  
29 (DMSO- $d_6$ , 101 MHz):  $\delta$  199.8, 153.4, 151.5, 145.4, 142.9, 138.4, 138.0, 134.8, 134.7, 134.1,  
30  
31 128.5, 127.5, 122.3, 105.8, 56.1, 47.6, 38.6, 25.7, 23.2. HRMS: (ESI,  $m/z$ ) Calcd for  $\text{C}_{36}\text{H}_{36}\text{N}_3\text{O}_9$   
32  
33  $[\text{M}+\text{H}]^+$ : 654.2452, found 654.2455.

### 43 **4.3 GSH dependent absorption spectra**

44  
45 Solutions of **HJTA** (100  $\mu\text{M}$ ) or **HJTB** (200  $\mu\text{M}$ ) were prepared with deionized water  
46  
47 containing 1% (v/v) DMSO with GSH (0 ~ 20 equiv) and cat. GST $\pi$ . All absorption spectra were  
48  
49 recorded at 37  $^\circ\text{C}$  for 0.5 h and scanning wavelength range was 350–700 nm with scanning speed  
50  
51 is 1.0 nm/s.

### 52 **4.4 GSH dependent emission spectra**

53  
54 Solutions (1.0  $\mu\text{M}$ ) of **HJTA** or **HJTB** were prepared in deionized water containing 1% (v/v)  
55  
56 DMSO with GSH (0 – 100  $\mu\text{M}$ ) and cat. GST $\pi$ . All emission spectra were performed at 37  $^\circ\text{C}$  for  
57  
58 0.5 h and excited at 440 nm and recorded from 450 nm to 650 nm.  
59  
60

#### 4.5 pH dependent absorption spectra

Solutions (100  $\mu\text{M}$ ) of **HJTA**, **HJTB** or **6** were prepared in deionized water containing 1% (v/v) DMSO with pH ranging from 7 to 3. All absorption spectra were recorded at room temperature (r.t.) and scanning wavelength range was 350–700 nm with scanning speed is 1.0 nm/s.

#### 4.6 pH dependent emission spectra

Solutions (1.0  $\mu\text{M}$ ) of **HJTA**, **HJTB** or **6** were prepared in deionized water containing 1% (v/v) DMSO with pH ranging from 7 to 3. All emission spectra were performed at r.t. and excited at 450 nm and recorded from 460 nm to 650 nm.

#### 4.7 Fluorescence selectivity evaluation

Solutions (1  $\mu\text{M}$ ) of **HJTA** with cat. GST $\pi$  and various biological analytes (Lys, His, Ala, Cys, Glu, Ser, Gly, Arg, H<sub>2</sub>O<sub>2</sub>, Ca<sup>2+</sup>, K<sup>+</sup>, Mg<sup>2+</sup>, Na<sup>+</sup>, Zn<sup>2+</sup>, Fe<sup>2+</sup>, Cu<sup>2+</sup>, Na<sub>2</sub>S, Al<sup>3+</sup>, Vc, NADH, GSH, 20  $\mu\text{M}$ ) were prepared at pH = 4.0 with deionized water containing 1% (v/v) DMSO at 37 °C for 0.5 h. All emission spectra were excited at 440 nm and recorded from 450 nm to 650 nm.

#### 4.8 Quantum efficiencies of fluorescence

The quantum yield of **HJTA** + GSH, **HJTA** at pH = 4.0 or **HJTB** at pH = 4.0 were determined in deionized water containing 1% (v/v) DMSO, using Quinine sulfate ( $\Phi_S = 0.55$  in 1 N H<sub>2</sub>SO<sub>4</sub>) as a reference.<sup>33</sup> The quantum yield was calculated according to Equation 1:

$$\Phi_X = \Phi_S (A_S F_X / A_X F_S) (n_X / n_S)^2 \quad (1)$$

$\Phi$ : quantum yield; A: absorbance at the excitation wavelength; F: integral area of fluorescence spectra at the same excitation wavelength; n: the refractive index of solvents; S and X represent the reference standard and unknown sample, respectively.

#### 4.9 Cell Culture

Human cancer cell lines (HT29 and HepG2) or normal cell lines (CCD841) were purchased from Shanghai Institute of Cell Biology (China), and murine gliosarcoma cell line (9L-2) was from department of neurological surgery tissue bank at University of California, San Francisco.

1  
2  
3  
4 These cell lines were routinely put in DMEM/RMPI 1640 medium possessing 10% FBS  
5  
6 (Invitrogen), 100 units/ml penicillin, and 100 units/ml streptomycin at 37 °C under an atmosphere  
7  
8 of 5% CO<sub>2</sub>.  
9

#### 10 **4.10 *In vitro* cellular uptake studies**

11  
12 For time dependent-cellular uptake: HT29 ( $2 \times 10^5$  cells/well) were seeded into 35 mm glass  
13  
14 bottom cell culture dishes respectively in 2.0 mL culture medium. After cell attachment, the  
15  
16 culture medium was replaced by the DMEM containing **HJTA** (1 μM) and the fluorescent images  
17  
18 were obtained every one minute for 60 minutes by Leica TCS SP5 LSM confocal microscope  
19  
20 using a 40X objective water lenses. The green fluorescence of **HJTA** was obtained by using a 405  
21  
22 nm laser. Filter set: 480-530 nm.  
23  
24

#### 25 **4.11 MTT assay**

26  
27 The in vitro antiproliferative effects were assessed on HT29, HepG2, 9L-2, and CCD841 by the  
28  
29 MTT method according to previous literature.<sup>44</sup> After washing the cells with PBS buffer, 0.5  
30  
31 mg/mL MTT solution was added and the cells were kept at 37 °C for 3 h. After MTT medium  
32  
33 removal, the formazan crystals were dissolved in DMSO and the absorbance was measured at 570  
34  
35 nm using a BioTek Microplate Absorbance Reader according to the protocol. The inhibitory effect  
36  
37 was expressed as percentage. Corresponding IC<sub>50</sub> values were then calculated through  
38  
39 corresponding software (GraphPadPrism Version 4.03).  
40

#### 41 **4.12 Intracellular fluorescence activation**

42  
43 HT29 and CCD841 cells ( $2 \times 10^5$  cells/well) were seeded into 35 mm glass bottom cell culture  
44  
45 dishes in 2.0 mL culture medium respectively. The cells were incubated in DMEM containing  
46  
47 **HJTA** (1 μM) with LysoTracker red DND-99 (1 μM) for 30 minutes. The fluorescent images  
48  
49 were obtained by Leica TCS SP5 LSM confocal microscope using a 40X objective water lenses.  
50  
51 The green fluorescence of **HJTA** was obtained by using a 405 nm laser. Filter set: 480-530 nm.  
52  
53 The red fluorescence of LysoTracker red was obtained by using a 561 nm laser. Filter set: 580-630  
54  
55 nm.  
56

#### 57 **4.13 Animals and tumor model**

1  
2  
3 All animal experimental protocols were approved by the Animal Research and Care Committee  
4 of Nantong University. To set up the subcutaneous tumor mouse model, female nude mice (5-6  
5 weeks old) were purchased from the Model Animal Research Center Affiliated to Nanjing  
6 University (Nanjing, China).  $1 \times 10^6$  HT29 or HT29/Luc cells were subcutaneously injected into  
7 the BALB/c mice. Animals bearing tumor were established (approximately 3 to 4 weeks) before  
8 used for fluorescence imaging.  
9

10  
11 To establish an orthotropic colon tumor model,  $1 \times 10^6$  luciferase-transfected HT29 cells  
12 (HT29/Luc) were directly injected into the upper part of the colons after anaesthesia in nude mice  
13 (5-6 weeks old). The tumor growth and development in mice were monitored by bioluminescent  
14 imaging. Two weeks later, the orthotropic colon tumors were successfully established.  
15

#### 23 **4.14 *Ex vivo* fluorescence imaging and tissue biodistribution**

24  
25 HT29 tumor-bearing mice were used for fluorescence imaging and before imaging, the  
26 tumor-bearing mice were intravenously (i.v.) injected with **HJTA** (40 mg/kg). First, the mice were  
27 placed onto the warmed stage inside of an IVIS light-tight chamber and anesthesia was maintained  
28 with 1% pentobarbital. All the image acquisitions were performed with Caliper IVIS Lumina II in  
29 vivo optical imaging system equipped with excitation filter: 465 nm and emission filter: GFP  
30 when the mice were anesthetized at 0 h, 1 h, 2 h, 4 h, 8 h, and 24 h postinjection. Then, the mice  
31 were sacrificed after imaging. The major organs including the heart, lung, liver, kidney, spleen,  
32 colon, and tumor were collected and imaged with the fluorescence imaging system as described  
33 above.  
34

#### 43 **4.15 Acute toxicity determination**

44  
45 The female ICR mice were randomly treated by intraperitoneal injection of a single dose of  
46 **HJTA** at 240.0, 300.0, 375.0, 468.8, and 585.9 mg/kg or vehicle control (n = 10 per group),  
47 respectively. The mice were monitored for their survival, body weights, behaviors, and movement  
48 abilities up to 14 days post treatment. The experimental protocols were evaluated and approved by  
49 the Nantong University Animal Care and Use Committee.  
50

#### 55 **4.16 *In vivo* tumor growth inhibition**

56  
57 All animal experimental protocols were approved by the Animal Research and Care Committee  
58 of Nantong University. Female BALB/c nude mice at the age of 5 to 6-week-old were inoculated  
59  
60

1  
2  
3 subcutaneously with  $1 \times 10^6$  HT29 cells. When tumor volumes reached  $100 \text{ mm}^3$ , the mice were  
4  
5 randomly administered with **HJTA**, COMC-6, and vehicle, respectively. The body weight of all  
6  
7 animals was monitored throughout the study and animals were euthanized if they incurred 20 %  
8  
9 weight loss between observations. Two axes (mm) of a tumor (L, longest axis; W, shortest axis)  
10  
11 were measured with a Vernier caliper. Tumor volume ( $\text{mm}^3$ ) was calculated using a formula of  
12  
13 'tumor volume =  $\frac{1}{2} (L \times W^2)$ '. Progression of tumors was monitored every 2 days up to 21 days  
14  
15 posttreatment. At the end of the experiment, the mice were sacrificed, and their tumors were  
16  
17 dissected out and weighed.

#### 19 **4.17 Cell apoptosis assay**

21 After 12h culture of HT29 cells, **HJTA** (0.4, 1.0, 2.5  $\mu\text{M}$ ), COMC-6 (2.5  $\mu\text{M}$ ), harmine (10  
22  
23  $\mu\text{M}$ ), or vehicle were incubated with the cells for 72 h. The cells were harvested and then stained  
24  
25 with APC-Annexin V and 7-AAD at 37 °C for 15 min. Flow cytometry analysis (Calibur, BD,  
26  
27 USA) was used to determine the percentage of apoptotic cells, using APC signal (FL4) (excitation  
28  
29  $\frac{1}{4}$  633 nm; emission  $\frac{1}{4}$  660 nm) and 7-AAD staining signal (FL3) (excitation  $\frac{1}{4}$  488 nm; emission  
30  
31  $\frac{1}{4}$  647 nm). The data were analyzed using WinList 3D (7.1) and the histogram was plotted using  
32  
33 Excel 2016.

#### 35 **4.18 Western blot analysis**

37  
38 The activities of apoptosis- and autophagy-related proteins were analyzed by the Western blot  
39  
40 assay. HT29 cells ( $1.5 \times 10^5$  /mL) were treated with or without vehicle, **HJTA**, COMC-6, or  
41  
42 harmine at indicated dosages for 72h. The cell lysates (0.05 mg/lane) were separated by  
43  
44 SDS-PAGE (12% gel) and transferred onto nitrocellulose membranes. When the reaction was  
45  
46 blocked using 5% non-fat milk, the target proteins were then detected by different antibodies, such  
47  
48 as anti-Bax, anti-Bcl-2, anti-cleaved-caspase 3, anti-cleaved-PARP, anti-p62, anti-LC3, anti-p62,  
49  
50 anti-beclin-1, and anti- $\beta$ -actin antibodies (Cell Signaling Technology, MA, USA), respectively.  
51  
52 The bound antibodies were detected by HRP-conjugated second antibodies and then visualized  
53  
54 using the chemiluminescent reagent.  
55  
56  
57  
58  
59  
60

**ASSOCIATED CONTENT****Supporting Information**

Supporting Information is available free of charge *via* the Internet at <http://pubs.acs.org>.

Molecular formula strings (CSV)

The pH-responsive spectroscopy properties, Calculations of pKa and pKa\*, GSH-responsive properties, time-dependent cellular uptake, relative quantum yield, <sup>1</sup>H & <sup>13</sup>C NMR spectra, HRMS and HPLC analysis.

**AUTHOR INFORMATION****Corresponding Author**

\*Tel.: +86-513-85051892; E-mail for Y. Ling: Lyyy111@sina.com, e-mail for Y.A. Zhang: zhangyanan@gmail.com.

**AUTHOR CONTRIBUTIONS**

# J. Liu and X. Liu contributed equally to this work.

**NOTES**

The authors declare no competing financial interest.

**ABBREVIATIONS USED**

Ala, alanine; Arg, arginine; Cys, cysteine; DMAP, 4-(*N,N*-dimethylamino)pyridine; DMF, dimethylformamide; DMSO, dimethyl sulfoxide; DNA, deoxyribonucleic acid; Glu, glutamic acid; Gly, glycine; GST, glutathione S-transferase; His, histidine; HRMS, high-resolution mass spectrometry; Lys, lysine; MS, mass spectrometry; NADH, reduced nicotinamide adenine dinucleotide; Ser, serine; ROS, reactive oxygen species; THF, tetrahydrofuran; TLC, thin-layer chromatography.

## ACKNOWLEDGEMENTS

This work was financially supported by the Natural Science Foundation of China (Nos. 31830028 & 21977058), China and Jiangsu Province Postdoctoral Science Foundation (2018T110533, 2016M590488, and 1601136B), the Project of “Jiangsu Six Peaks of Talent” (2016-SWYY-CXTD-008 and 2014-SWYY-044), the Project of “Jiangsu 333 high-level talents”, Jiangsu Province Innovation Project of Postgraduate Training (KYCX19\_2086), and Applied Research Projects of Nantong City (MS12018079 and JC2018125).

## REFERENCES

- (1) Wu, T.; Dai, Y. Tumor Microenvironment and Therapeutic Response. *Cancer Lett.* **2017**, *387*, 61-68.
- (2) Junttila, M. R.; de Sauvage, F. J. Influence of Tumour Micro-Environment Heterogeneity on Therapeutic Response. *Nature* **2013**, *501* (7467), 346-354.
- (3) Ngabire, D.; Kim, G. D. Autophagy and Inflammatory Response in the Tumor Microenvironment. *Int. J. Mol. Sci.* **2017**, *18* (9), 2016.
- (4) Quail, D. F.; Joyce, J. A. Microenvironmental Regulation of Tumor Progression and Metastasis. *Nat. Med.* **2013**, *19* (11), 1423-1437.
- (5) Feng, L.; Xie, R.; Wang, C.; Gai, S.; He, F.; Yang, D.; Yang, P.; Lin, J. Magnetic Targeting, Tumor Microenvironment-Responsive Intelligent Nanocatalysts for Enhanced Tumor Ablation. *ACS Nano* **2018**, *12* (11), 11000-11012.
- (6) Song, Q.; Yin, Y.; Shang, L.; Wu, T.; Zhang, D.; Kong, M.; Zhao, Y.; He, Y.; Tan, S.; Guo, Y.; Zhang, Z. Tumor Microenvironment Responsive Nanogel for the Combinatorial Antitumor Effect of Chemotherapy and Immunotherapy. *Nano Lett.* **2017**, *17* (10), 6366-6375.
- (7) Zhang, P.; Wang, J.; Chen, H.; Zhao, L.; Chen, B.; Chu, C.; Liu, H.; Qin, Z.; Liu, J.; Tan, Y.; Chen, X.; Liu, G. Tumor Microenvironment-Responsive Ultrasmall Nanodrug Generators with Enhanced Tumor Delivery and Penetration. *J. Am. Chem. Soc.* **2018**, *140* (44), 14980-14989.
- (8) Nie, X.; Liang, L.; Xi, H.; Jiang, S.; Jiang, J.; Tang, C.; Liu, X.; Liu, S.; Wan, C.; Zhao, J.; Yang, J. 2,3,7,8-Tetrachlorodibenzo-p-dioxin induces premature senescence of astrocytes via WNT/ $\beta$ -catenin signaling and ROS production. *J. Appl. Toxicol.* **2015**, *35*, 851-860.
- (9) Liu, Z.; Romero-Canelon, I.; Qamar, B.; Hearn, J. M.; Habtemariam, A.; Barry, N. P.; Pizarro, A. M.; Clarkson, G. J.; Sadler, P. J. The Potent Oxidant Anticancer Activity of Organoiridium Catalysts. *Angew. Chem. Int. Ed.* **2014**, *126* (15), 4022-4027.
- (10) Qiao, C.; Yang, J.; Shen, Q.; Liu, R.; Li, Y.; Shi, Y.; Chen, J.; Shen, Y.; Xiao, Z.; Weng, J. Traceable Nanoparticles with Dual Targeting and ROS Response for RNAi-Based Immunotherapy of Intracranial Glioblastoma Treatment. *Adv. Mater.* **2018**, 1705054.

- 1
- 2
- 3
- 4 (11) Chen, D.; Zhang, G.; Li, R.; Guan, M.; Wang, X.; Zou, T.; Zhang, Y.; Wang, C.; Shu, C.; Hong, H.; Wan, L. J. Biodegradable, Hydrogen Peroxide, and Glutathione Dual Responsive Nanoparticles for Potential Programmable Paclitaxel Release. *J. Am. Chem. Soc.* **2018**, *140* (24), 7373-7376.
- 5
- 6 (12) Yin, G.; Niu, T.; Yu, T.; Gan, Y.; Sun, X.; Yin, P.; Chen, H.; Zhang, Y.; Li, H.; Yao, S. Simultaneous Visualization of Endogenous Homocysteine, Cysteine, Glutathione, and their Transformation through Different Fluorescence Channels. *Angew. Chem. Int. Ed. Engl.* **2019**, *58* (14), 4557-4561.
- 7
- 8 (13) Gao, M.; Yu, F.; Lv, C.; Choo, J.; Chen, L. Fluorescent Chemical Probes for Accurate Tumor Diagnosis and Targeting Therapy. *Chem. Soc. Rev.* **2017**, *46* (8), 2237-2271.
- 9
- 10 (14) Chatterjee, A.; Gupta, S. The Multifaceted Role of Glutathione S-Transferases in Cancer. *Cancer Lett.* **2018**, *433*, 33-42.
- 11
- 12 (15) di Ilio, C.; Sacchetta, P.; del Boccio, G.; la Rovere, G.; Federici, G. Glutathione Peroxidase, Glutathione S-Transferase and Glutathione Reductase Activities in Normal and Neoplastic Human Breast Tissue. *Cancer Lett.* **1985**, *29* (1), 37-42.
- 13
- 14 (16) Hengstler, J. G.; Bottger, T.; Tanner, B.; Dietrich, B.; Henrich, M.; Knapstein, P. G.; Junginger, T.; Oesch, F. Resistance Factors in Colon Cancer Tissue and the Adjacent Normal Colon Tissue: Glutathione S-Transferases Alpha and Pi, Glutathione and Aldehyde Dehydrogenase. *Cancer Lett.* **1998**, *128* (1), 105-112.
- 15
- 16 (17) Townsend, D. M.; Tew, K. D. The Role of Glutathione-S-Transferase in Anti-cancer Drug Resistance. *Oncogene* **2003**, *22* (47), 7369-7375.
- 17
- 18 (18) Aghil, O.; Bibby, M. C.; Carrington, S. J.; Double, J.; Douglas, K. T.; Phillips, R. M.; Shing, T. K. Synthesis and Cytotoxicity of Shikimate Analogues. Structure: Activity Studies Based on 1-Crotonyloxymethyl-3R,4R,5R-Trihydroxycyclohex-2-Enone. *Anticancer Drug Des.* **1992**, *7* (1), 67-82.
- 19
- 20 (19) Hamilton, D. S.; Ding, Z.; Ganem, B.; Creighton, D. J. Glutathionyl Transferase Catalyzed Addition of Glutathione to COMC: A New Hypothesis for Antitumor Activity. *Org. Lett.* **2002**, *4* (7), 1209-1212.
- 21
- 22 (20) Hamilton, D. S.; Zhang, X.; Ding, Z.; Hubatsch, I.; Mannervik, B.; Houk, K. N.; Ganem, B.; Creighton, D. J. Mechanism of the Glutathione Transferase-Catalyzed Conversion of Antitumor 2-Crotonyloxymethyl-2-Cycloalkenones to GSH Adducts. *J. Am. Chem. Soc.* **2003**, *125* (49), 15049-15058.
- 23
- 24 (21) Lin, B.; Chen, H.; Liang, D.; Lin, W.; Qi, X.; Liu, H.; Deng, X. Acidic pH and High-H<sub>2</sub>O<sub>2</sub> Dual Tumor Microenvironment-Responsive Nanocatalytic Graphene Oxide for Cancer Selective Therapy and Recognition. *ACS Appl. Mater. Inter.* **2019**, *11* (12), 11157-11166.
- 25
- 26 (22) Kong, C.; Li, Y.; Liu, Z.; Ye, J.; Wang, Z.; Zhang, L.; Kong, W.; Liu, H.; Liu, C.; Pang, H.; Hu, Z.; Gao, J.; Qian, F. Targeting the Oncogene KRAS Mutant Pancreatic Cancer by Synergistic Blocking of Lysosomal Acidification and Rapid Drug Release. *ACS Nano* **2019**, *13* (4), 4049-4063.
- 27
- 28 (23) Ma, W.; Ge, X.; Xu, Z.; Zhang, S.; He, X.; Li, J.; Xia, X.; Chen, X.; Liu, Z. Theranostic Lysosomal Targeting Anticancer and Antimetastatic Agents: Half-Sandwich Iridium(III) Rhodamine Complexes. *ACS omega* **2019**, *4* (12), 15240-15248.
- 29
- 30 (24) Zhao, Z.; Meng, H.; Wang, N.; Donovan, M. J.; Fu, T.; You, M.; Chen, Z.; Zhang, X.; Tan, W. A Controlled-Release Nanocarrier with Extracellular pH Value Driven Tumor Targeting and Translocation for Drug Delivery. *Angew. Chem. Int. Ed. Engl.* **2013**, *52* (29), 7487-7491.
- 31
- 32 (25) Estrella, V.; Chen, T.; Lloyd, M.; Wojtkowiak, J.; Cornnell, H. H.; Ibrahim-Hashim, A.; Bailey, K.; Balagurunathan, Y.; Rothberg, J. M.; Sloane, B. F.; Johnson, J.; Gatenby, R. A.; Gillies, R. J. Acidity Generated by the Tumor Microenvironment Drives Local Invasion. *Cancer Res.* **2013**, *73* (5), 1524-1535.
- 33
- 34 (26) Webb, B. A.; Chimentì, M.; Jacobson, M. P.; Barber, D. L. Dysregulated pH: A Perfect Storm for Cancer Progression. *Nat. Rev. Cancer* **2011**, *11* (9), 671-677.
- 35
- 36 (27) Tredan, O.; Galmarini, C. M.; Patel, K.; Tannock, I. F. Drug Resistance and the Solid Tumor Microenvironment. *J. Natl. Cancer Inst.* **2007**, *99* (19), 1441-1454.
- 37
- 38 (28) Han, J.; Burgess, K. Fluorescent Indicators for Intracellular pH. *Chem. Rev.* **2010**, *110* (5), 2709-27028.
- 39
- 40 (29) Uthaman, S.; Huh, K. M.; Park, I. K. Tumor Microenvironment-Responsive Nanoparticles for Cancer Theragnostic Applications. *Biomater. Res.* **2018**, *22*, 22.
- 41
- 42 (30) Ling, Y.; Xu, C.; Luo, L.; Cao, J.; Ling, X. Novel  $\beta$ -Carboline/Hydroxamic Acid Hybrids Targeting Both Histone Deacetylase and DNA Display High Anticancer Activity via Regulation of the P53 Signaling Pathway. *J. Med. Chem.* **2015**, *58* (23), 9214-9227.
- 43
- 44 (31) Kovvuri, J.; Nagaraju, B.; Nayak, V. L.; Akunuri, R.; Rao, M. P. N.; Ajitha, A.; Nagesh, N.; Kamal, A. Design, Synthesis and Biological Evaluation of New Beta-Carboline-Bisindole Compounds as DNA Binding, Photocleavage Agents and Topoisomerase I Inhibitors. *Eur. J. Med. Chem.* **2018**, *143*, 1563-1577.
- 45
- 46 (32) Kamal, A.; Sathish, M.; Nayak, V. L.; Srinivasulu, V.; Kavitha, B.; Tangella, Y.; Thummuri, D.; Bagul, C.; Shankaraiah, N.; Nagesh, N. Design and Synthesis of Dithiocarbamate Linked Beta-Carboline Derivatives: DNA Topoisomerase II Inhibition with DNA Binding and Apoptosis Inducing Ability. *Bioorg. Med. Chem.* **2015**, *23* (17), 5511-5526.
- 47
- 48 (33) Melhuish, H.W. Quantum Efficiencies of Fluorescence of Organic Substances: Effect of Solvent and Concentration of the Fluorescent Solute. *J. Phys. Chem.* **1961**, *65* (2), 229-235.
- 49
- 50 (34) O'Brien, M. L.; Tew, K. D. Glutathione and Related Enzymes in Multidrug Resistance. *Eur. J. Cancer* **1996**, *32A* (6), 967-978.
- 51
- 52 (35) Wang, Q.; Ju, X.; Wang, J.; Fan, Y.; Ren, M.; Zhang, H. Immunogenic Cell Death in Anticancer Chemotherapy and Its Impact on Clinical Studies. *Cancer Lett.* **2018**, *438*, 17-23.
- 53
- 54 (36) Ni, H.; Xia, C.; Zhao, Y. Synthesis, cytotoxicity and pro-apoptosis activity of isoquinoline. *Med. Chem. Res.* **2017**, *26* (11), 2861-2869.
- 55
- 56
- 57
- 58
- 59
- 60

- 1  
2  
3 (37) Huang, Q.; Li, F.; Liu, X.; Li, W.; Shi, W.; Liu, F. F.; O'Sullivan, B.; He, Z.; Peng, Y.; Tan, A. C.; Zhou, L.;  
4 Shen, J.; Han, G.; Wang, X. J.; Thorburn, J.; Thorburn, A.; Jimeno, A.; Raben, D.; Bedford, J. S.; Li, C. Y.  
5 Caspase 3-Mediated Stimulation of Tumor Cell Repopulation During Cancer Radiotherapy. *Nat. Med.* **2011**,  
6 *17* (7), 860-866.
- 7 (38) Sun, F.; Jiang, X.; Wang, X.; Bao, Y.; Feng, G.; Liu, H.; Kou, X.; Zhu, Q.; Jiang, L.; Yang, Y. Vincristine  
8 ablation of Sirt2 induces cell apoptosis and mitophagy via Hsp70 acetylation in MDA-MB-231 cells. *Biochem.*  
9 *Pharmacol.* **2019**, *162*, 142-153.
- 10 (39) Zhong, Z.; Sanchez-Lopez, E.; Karin, M. Autophagy, Inflammation, and Immunity: A Troika Governing  
11 Cancer and Its Treatment. *Cell* **2016**, *166* (2), 288-298.
- 12 (40) Wang, F.; Ma, H.; Liu, Z.; Huang, W.; Xu, X.; Zhang, X. alpha-Mangostin inhibits DMBA/TPA-induced skin  
13 cancer through inhibiting inflammation and promoting autophagy and apoptosis by regulating  
14 PI3K/Akt/mTOR signaling pathway in mice. *Biomed. Pharmacother.* **2017**, *92*, 672-680.
- 15 (41) Lu, Y.; Zhang, R.; Liu, S.; Zhao, Y.; Gao, J.; Zhu, L. ZT-25, a new vacuolar H(+)-ATPase inhibitor, induces  
16 apoptosis and protective autophagy through ROS generation in HepG2 cells. *Eur. J. Pharmacol.* **2016**, *15*,  
17 130-138.
- 18 (42) Ling, Y.; Gao, W. J.; Ling, C.; Liu, J.; Meng, C.; Qian, J.; Liu, S.; Gan, H.; Wu, H.; Tao, J.; Dai, H.; Zhang, Y.  
19  $\beta$ -Carboline and N-hydroxycinnamamide Hybrids as Anticancer Agents for Drug-Resistant Hepatocellular  
20 Carcinoma. *Eur. J. Med. Chem.* **2019**, *168*, 515-526.
- 21 (43) Kotoku, N.; Sumii, Y.; Kobayashi, M. Stereoselective Synthesis of Core Structure of Cortistatin A. *Org. Lett.*  
22 **2011**, *13* (13), 3514-3517.
- 23 (44) Zou, Y.; Zhao, D.; Yan, C.; Ji, Y.; Liu, J.; Xu, J.; Lai, Y.; Tian, J.; Zhang, Y.; Huang, Z. Novel  
24 Ligustrazine-Based Analogs of Piperlongumine Potently Suppress Proliferation and Metastasis of Colorectal  
25 Cancer Cells in Vitro and in Vivo. *J. Med. Chem.* **2018**, *61* (5), 1821-1832.
- 26  
27  
28  
29  
30  
31  
32  
33  
34  
35  
36  
37  
38  
39  
40  
41  
42  
43  
44  
45  
46  
47  
48  
49  
50  
51  
52  
53  
54  
55  
56  
57  
58  
59  
60

## Table of Contents graphic

